2014

Hf–Co and Zr–Co alloys for rare-earth-free permanent magnets

Balamurugan Balasubramanian
University of Nebraska-Lincoln, balamurugan@unl.edu

Bhaskar Das
University of Nebraska-Lincoln, bhaskar.das@huskers.unl.edu

Wenyong Zhang
University of Nebraska-Lincoln, wenyong.zhang@unl.edu

Ralph Skomski
University of Nebraska at Lincoln, rskomski2@unl.edu

David J. Sellmyer
University of Nebraska-Lincoln, dsellmyer@unl.edu

Published in *Journal of Physics: Condensed Matter* 26:6 (2014), 064204 (8 pp.); doi:10.1088/0953-8984/26/6/064204

Submitted July 10, 2013; revised August 20, 2013; published January 27, 2014.

Hf–Co and Zr–Co alloys for rare-earth-free permanent magnets

B. Balamurugan, B. Das, W. Y. Zhang, R. Skomski, and D. J. Sellmyer

Nebraska Center for Materials and Nanoscience and Department of Physics and Astronomy, University of Nebraska, Lincoln, NE 68588, USA

Corresponding authors – B. Balamurugan, email bbalasubramanian2@unl.edu and D. J. Sellmyer, email dsellmyer@unl.edu

Abstract

The structural and magnetic properties of nanostructured Co-rich transition-metal alloys, $Co_{100-x}TM_x$ (TM = Hf, Zr and $10 \le x \le 18$), were investigated. The alloys were prepared under nonequilibrium conditions using cluster-deposition and/or melt-spinning methods. The high-anisotropy $HfCo_7$ and Zr_2Co_{11} structures were formed for a rather broad composition region as compared to the equilibrium bulk phase diagrams, and exhibit high Curie temperatures of above 750 K. The composition, crystal structure, particle size, and easy-axis distribution were precisely controlled to achieve a substantial coercivity and magnetization in the nanostructured alloys. This translates into high energy products in the range of about 4.3–12.6 MGOe, which are comparable to those of alnico.

1. Introduction

The science and technology of developing new magnetic materials for energy production and transportation are critical in response to the most significant worldwide challenges on energy and environmental security.[1–4] This is mainly owing to the critical-material aspects of rare-earth elements and an ever-increasing demand of permanent magnets in a wide range of applications. Besides having a high Curie temperature T_c, a permanent-magnet material must also exhibit a high energy product $(BH)_{max}$, the maximum of the product of the magnetic field induction B and the magnetic field H in the second quadrant of the BH curve.[5–7] $(BH)_{max}$ is generally related to the remanent magnetization M_r, and coercivity H_c,

which basically originates from the magnetocrystalline anisotropy K_1. Theoretically, the maximum possible energy product is $(BH)_{max} = J^2_s/4$, when a magnet exhibits a square M–H loop with a M_r equal to the saturation magnetization M_s ($J_s = 4\pi M_s$ is the saturation magnetic polarization) and a coercivity greater than $M_s/2$.[5–11]

Mn-based alloys such as MnBi, MnAl, and MnGa and $L1_0$-ordered FePt are widely investigated rare-earth-free permanent-magnet materials due to their high K_1 and T_c values.[12–17] The Mn-based alloys, however, exhibit relatively low $(BH)_{max}$ values (4.7–7.7 MGOe) as compared to alnico (≈ 10 MGOe) and rare-earth-based magnets such as Nd–Fe–B (≈ 60 MGOe) and Sm–Co (≈ 30 MGOe) and this is mainly due to their low J_s in the range of 5.9– 7.5 kG.[3, 12–17] $L1_0$-ordered FePt have shown $(BH)_{max}$ up to 54 MGOe, but the high cost of Pt is a limiting factor for bulk applications.[11, 18] Recently there has been an intensified research on Co-rich transition-metal alloys such as $HfCo_7$ and Zr_2Co_{11} crystallizing in noncubic high-anisotropy structures to develop new rare-earth-free magnetic materials with high energy products.[19–27] However, as shown in the equilibrium Co–Hf phase diagram (figure 1(a)), the metastable nature and/or the requirement of high formation temperature of about 1050–1230°C for $HfCo_7$ phase indicate that a precise control of the composition and a rapid cooling process after the alloy formation are required to obtain the phase purity.[28] Although the Co–Zr phase diagram shows Zr_2Co_{11} phase for the temperature range of about 300–1254°C at about 15.4 at.% of Zr as shown in figure 1(b),[29] a high-temperature growth or annealing process followed by a rapid quenching/cooling was generally used to obtain high-anisotropy crystal structures in the bulk alloys.[19–23]

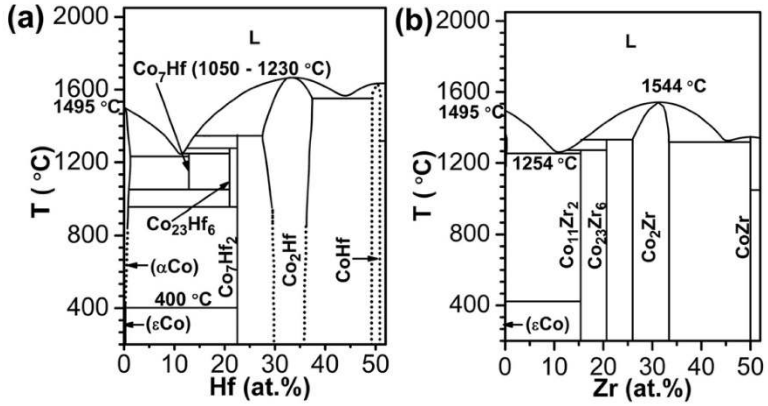

Figure 1. Binary phase diagrams: (a) Co–Hf[28] and (b) Co–Zr.[29]

Melt spinning and gas-aggregation-type cluster deposition, in which the alloy formation and crystallization process occur in nonequilibrium conditions, have been shown to be promising methods for the synthesis of nanostructured $HfCo_7$ and Zr_2Co_{11} alloys.[19, 20, 24–26] A rapid cooling process during the melt spinning helps to reduce substantially the formation of secondary phases.[19, 20] In comparison, nanoparticles smaller than 10 nm can be directly ordered during the gas-aggregation process using a cluster-deposition method, without the requirement of a high-temperature annealing, and this process also facilitates

the alignment of the easy axes prior to deposition, when applying a magnetic field.[25, 26, 30] In this study, we present the structural and magnetic properties of nanocrystalline $Co_{100-x}TM_x$ (TM = Hf, Zr) bulk alloys with varying compositions $10 \le x \le 18$ prepared using melt spinning, and the results are compared with those of cluster-deposited nanoparticles using $Co_{100-x}Hf_x$ system as a typical example. We emphasize the need to control composition, particle size, exchange interactions, and nanostructuring including the easy-axis alignment and compaction to obtain high energy products in the nanostructured alloys.

2. Experimental methods

Nanocrystalline $Co_{100-x}TM_x$ alloys (TM = Zr, Hf and $10 \le x \le 18$) were prepared using melt spinning.[19, 24] For this, a conventional arc-melting process was used to prepare alloys having the desired compositions from the pure elements.[19, 20] Following this, arc-melted alloys are remelted to a molten state in a quartz tube and subsequently ejected on the surface of a rotating copper wheel to form nanocrystalline ribbons.

In the case of cluster deposition,[26, 31] a composite target was sputtered using a direct-current magnetron discharge into a water-cooled gas-aggregation chamber to form crystalline $Co_{100-x}Hf_x$ ($10 \le x \le 18$) nanoparticles, which were extracted toward the substrate kept at room temperature in a deposition chamber. The composition of the $Co_{100-x}Hf_x$ nanoparticles was varied by mainly controlling the stoichiometry of the sputtering target. The nanoparticle samples were capped with a thin SiO_2 cap layer immediately after deposition using a radiofrequency magnetron sputtering gun employed in the deposition chamber. This is necessary to prevent the oxidation of nanoparticle samples on exposure to air.

X-ray diffraction (XRD: Rigaku D/MaxB diffractometer), scanning electron microscope (SEM: FEI Nova NanoSEM450 and JEOL JSM 840A scanning electron microscope for EDX analysis), and transmission electron microscope (TEM: FEI Tecnai Osiris) measurements were carried out to investigate the structural properties. A superconducting quantum interference device (SQUID) magnetometer and a physical property measurement system (PPMS) from Quantum Design were used for magnetic characterization. Note that the nanoparticles were deposited with low coverage densities on carbon-coated copper grids for TEM measurements. For XRD and SQUID measurements, dense-packed nanoparticle films were fabricated on Si(001) substrates.

3. Results and discussion

The surface speed of the copper wheel was varied from 25 to 70 m s^{-1} to increase the cooling rate during the melt-spinning process, which reduces the grain size and also improves the phase purity. For example, the structural and magnetic properties of the melt-spun $Co_{84}Zr_{16}$ ribbons prepared at two different wheel speeds (45 and 70 m s^{-1}) are presented in figure 2. TEM images, as shown in figures 2(a) and (b), reveal that the melt-spun ribbons are nanocrystalline, and also show a decrease in the average grain size from about 120 to 50 nm on increasing the wheel speed from 45 to 70 m s^{-1}. The corresponding XRD patterns are shown in figure 2(c). Although the Zr_2Co_{11} phase corresponds to 15.4 at.% of Zr in the

equilibrium Co–Zr phase diagram, the Zr_2Co_{11} compound is often obtained for stoichiometry corresponding to $ZrCo_{5.1}$.[20] The crystal structure of Zr_2Co_{11} also remains elusive and under dispute.[19–23] Zr_2Co_{11} is, however, reported to crystallize in orthorhombic or rhombohedral structures.[21] In the present study, the XRD patterns of the nanocrystalline Co84Zr16 ribbons have intense XRD peaks corresponding to both rhombohedral and orthorhombic Zr_2Co_{11} structures, in addition to only a very weak-intensity peak of the cubic Zr_6Co_{23} phase as shown in figure 2(c). This result shows that $Co_{84}Zr_{16}$ ribbons are predominantly Zr_2Co_{11}.

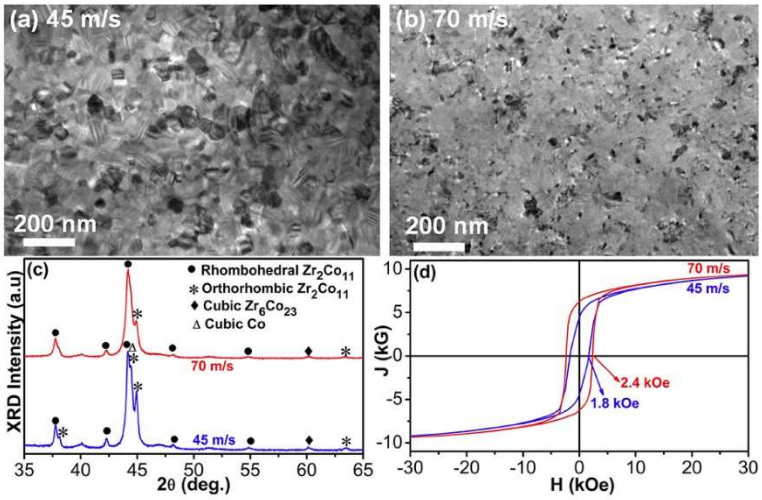

Figure 2. Melt-spun nanocrystalline $Co_{84}Zr_{16}$ alloys prepared at different wheel speeds (45 and 70 m s^{-1}): (a) and (b) TEM micrographs. (c) XRD patterns. (d) Room-temperature hysteresis loops.

In addition to Zr_2Co_{11} and Z_6Co_{23} phases, generally the melt-spun Zr–Co ribbons also contain cubic Co, which is difficult to be quantified using XRD patterns. This is mainly due to the coincidence of the peak position of the most intense XRD peak corresponding to the cubic Co with the XRD peaks of the predominant Zr_2Co_{11} phase as indicated in figure 2(c). Thermomagnetic measurements, however, showed only a small fraction of Co in the melt-spun Zr–Co ribbons, which is about 1.5–7.0 vol.% and depends on wheel speed and the stoichiometry of the ribbons.[19] It is also worth noting that the rhombohedral structure is reported to form first during the solidification process and subsequently transforms to orthorhombic structure at low temperatures.[21] In agreement with this, an improvement of the cooling rate on increasing the wheel speed improves the content of the rhombohedral Zr_2Co_{11} as compared to that of orthorhombic Zr_2Co_{11} as shown by the relative changes in the intensity of the XRD peaks of the corresponding structures in figure 2(c). In addition, the relative intensity changes of the XRD patterns of $Co_{84}Zr_{16}$ alloys also indicate that the contents of Co and Zr_6Co_{23} decrease on increasing the wheel speed from 45 to 70 m s^{-1}.

The M–H loops measured along the long axis (ribbon direction) for the $Zr_{16}Co_{84}$ ribbons at 300 K are shown in figure 2(d) and reveal the following results. First, the shape of the

M–H loop for the $Zr_{16}Co_{84}$ alloys prepared at 45 m s^{-1} clearly suggests the presence of soft phases, which are probably Co and Zr_6Co_{23} as revealed by the XRD results. On increasing the wheel speed to 70 m s^{-1}, the M–H loop exhibits nearly a single-phase behavior and also shows an increase of coercivity (H_c) to 2.4 kOe. This result can be attributed to a substantial decrease of the content of the soft phases such as Co and Zr_6Co_{23}. Second, M does not saturate completely even for H = 70 kOe (not shown in figure 2(d)), indicating high magnetocrystalline anisotropies in the samples. The law-of-approach to saturation method was used to evaluate K_1 and J_s.[7, 32] For example, this analysis yields a high K_1 = 13.5 Mergs cm^{-3} and a high J_s = 9.7 kG for the nanocrystalline $Co_{84}Zr_{16}$ alloy prepared at 70 m s^{-1}. From this, the magnetic anisotropy field HA is estimated to be 34.9 kOe using the relation $H_A = 2K_1/M_s$ and this result is consistent with the reported value of about 34 kOe for Zr_2Co_{11}.[22] Similarly, the structural and magnetic properties were tailored for the melt-spun $HfCo_7$ alloys having orthorhombic structure by varying the wheel speed, and a high $K_1 \approx$ 19:4 Mergs cm^{-3} was obtained with J_s = 11.8 kG and H_c = 2.4 kOe for a wheel speed of about 40 m s^{-1}. In the case of orthorhombic $HfCo_7$, we also have evaluated the magnetic properties using density-functional calculations, and this analysis yields a K_1 = 16.7 Mergs cm^{-3} and J_s = 11.4 kG, which are in good agreement with the experimental results.[24] Zr_2Co_{11} and $HfCo_7$ exhibit magnetic anisotropies comparable with those of Mn-based alloys, but J_s is higher and comparable with that of $SmCo_5$ ($J_s \approx$ 10.7 kG).[9, 12]

According to the equilibrium phase diagrams, the intermetallic $HfCo_7$ and Zr_2Co_{11} phases generally form for ideal compositions of about 12.5 Hf at.% and 15.4 at.% Zr, respectively.[28, 29] We have investigated the structural stability of $HfCo_7$ and Zr_2Co_{11} in the nanocrystalline $Co_{100-x}Hf_x$ and $Co_{100-x}Zr_x$ alloys respectively by varying the value of x close to the corresponding ideal compositions. Figure 3(a) shows the XRD patterns of the nanocrystalline $Co_{100-x}Hf_x$ with x varying from 11.0 to 16.7 at.%. The standard positions of x-ray diffraction peaks corresponding to orthorhombic $HfCo_7$ and cubic $HfCo_2$ are shown as red and blue vertical lines, respectively, in figure 3(a).[24, 33, 34] For compositions x = 11.0 and 12.5 at.%, the positions of the x-ray diffraction peaks are in good agreement with the standard data corresponding to the orthorhombic $HfCo_7$ phase.[24] XRD patterns for x = 14.6 and 16.7 at.% also show all the intense diffraction peaks corresponding to $HfCo_7$, but they also exhibit a weak hump at $2\theta \approx 43.5°$ and a new peak at $2\theta \approx 37.5°$, closer to the standard data of the most intense diffraction peaks of the cubic $HfCo_2$ phase.[33, 34] This result is also supported by the appreciable H_c (2.0–2.4 kOe) and J_s (8.9–11.8 kG) observed at 300 K in the composition ranges indicated by the black-dotted rectangle in figure 3(b), where the major phase is high-anisotropy $HfCo_7$.

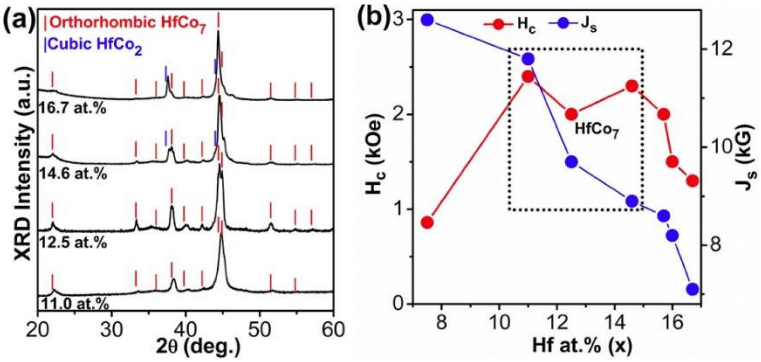

Figure 3. Melt-spun nanocrystalline $Co_{100-x}Hf_x$ alloys prepared at a wheel speed of 40 m s^{-1}. (a) XRD patterns, where the standard XRD peak positions for orthorhombic $HfCo_7$ and cubic $HfCo_2$ are given as red and blue vertical lines, respectively.[24, 33, 34] (b) Coercivity H_c and saturation magnetic polarization J_s at 300 K as a function of x. The dotted rectangle represents the composition ranges having major high-anisotropy $HfCo_7$ phase.

Similarly, the nanocrystalline $Co_{100-x}Zr_x$ alloys with $15.0 \le x \le 16.5$ reported in the present study show predominant high-anisotropy Zr_2Co_{11} phase and exhibit H_c (0.5–2.5 kOe) and J_s (9.7–10.3 kG) at 300 K (not shown in figure 3). Further, Zr_2Co_{11} phase with about 86 vol.% was obtained in the melt-spun $Co_{100-x}Zr_x$ ribbons even for a high $x = 21$.[19] Note that Zr_6Co_{23} phase is the favorable phase for $x = 21$ according to the Co–Zr phase diagram, and thus the extended stability of the Zr_2Co_{11} phase observed in the present study can be attributed as due to the nonequilibrium melt-spinning process.

As already explained, a high T_c and a high $(BH)_{max}$ are key figures of merit for a permanent-magnet material. The M–T curves for the nanocrystalline melt-spun $HfCo_7$ and Zr_2Co_{11} alloys are shown in figures 4(a) and (b), respectively. The experimental M does not reach zero for a high temperature of about 900 K, and has a nonzero tail. This is presumably due to the presence of Co, which has a high T_c = 1388 K.[6, 35] To fit the experimental data, we have used the implicit equation

$$T(m, h) = (1-m^{1/B})^{2/3} + h/m, \quad (1)$$

where $m = (M - M_{Co})/(M_0 - M_{Co})$ is the reduced normalized magnetization after removing the Co background or contribution of cobalt to the total magnetization (M_{Co}). M_0 is the T = 0 magnetization, $t = T/T_c$, and B describes the magnetization contribution from Bloch's law.[36, 37] Furthermore, $h \sim H/H_{MF}$ is a magnetic field parameter, where H_{MF} is the molecular field. At low temperatures, equation (1) reproduces Bloch's law $M = M_s(1 - B(T/T_c)^{3/2})$.[36, 37] Near T_c, the critical behavior is reproduced slightly better than that obtained by the mean-field approximation, with a critical exponent $\beta = B \approx 0.3$. Above T_c, it reproduces the Curie-Weiss law, $M \sim H/(T - T_c)$.

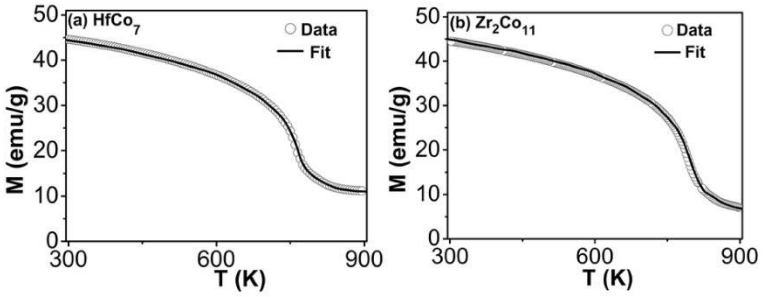

Figure 4. Temperature-dependent magnetization (M–T) curves measured in a magnetic field H = 1 kOe for melt-spun alloys: (a) $HfCo_7$. (b) Zr_2Co_{11}. The experimental data were fitted to evaluate the Curie temperature T_c using equation (1).

Figures 4(a) and (b) compare the predictions from equation (1) with the experimental data. For $HfCo_7$, figure 4(a), the fit yields T_c = 751 K; M_0 = 47.2 emu g^{-1}, and M_{Co} = 9.5 emu g^{-1}. For Zr_2Co_{11}, the values are T_c = 783 K; M_0 = 47.3 emu g^{-1}, and M_{Co} = 4.8 emu g^{-1} (figure 4(b)). Note that equation (1) is approximate but reproduces the experimental data with a remarkable accuracy. The main reason is the structure of the Landau free energy $F(M)$, which is approximately linear in $T - T_c$ but generally exhibits a very complicated and difficult to invert dependence on M. Note that T_c = 751 K ($HfCo_7$) and T_c = 783 K (Zr_2Co_{11}) are consistent with the reported T_c for Hf–Co and Zr–Co based alloys, respectively.[22, 27]

The rare-earth-free Co-rich intermetallic compounds exhibit a high J_s of about 11.8 kG ($HfCo_7$) and 9.7 kG (Zr_2Co_{11}) at 300 K, which can theoretically yield maximum energy products of about 34.8 and 23.5 MGOe, respectively. We have determined the energy products from the room temperature B and (BH_i) curves for the nanocrystalline melt-spun $HfCo_7$ (figure 5(a)) and Zr_2Co_{11} (figure 5(b)). $H_i = H - NM_s$ is the internal field, where N is the demagnetization factor and is ideally zero for the nanocrystalline ribbon samples measured along the long axis. We have also estimated N to be zero along the ribbon directions by comparing the slopes (micromagnetic susceptibilities) of the in-plane and out-of-plane M–H curves.[5, 6, 47] Figures 5(a) and (b) yield only moderate $(BH_i)_{max}$ values of 4.3 MGOe ($HfCo_7$) and 5.2 MGOe (Zr_2Co_{11}), and these values are much lower than the above-mentioned corresponding theoretical maximum. This is mainly due to the low remanent magnetization of $HfCo_7$ (M_r/M_s = 0.59) and Zr_2Co_{11} (M_r/M_s = 0.64). Generally M_r/M_s for a uniaxially isotropic crystal is about 0.50 and a small increase of M_r/M_s observed in the nanocrystalline ribbons is probably due to the exchange interaction between the magnetic grains. However, an alignment of easy axes in $HfCo_7$ and Zr_2Co_{11} alloys is highly desirable to obtain a further increase of M_r/M_s and subsequently to improve the energy products.

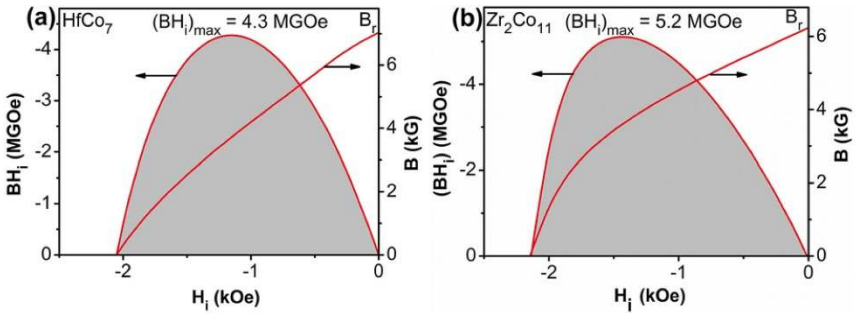

Figure 5. Room temperature B and BH_i curves as a function of H_i for the melt-spun isotropic alloys: (a) $HfCo_7$ and (b) Zr_2Co_{11}.

As compared to the melt spinning, cluster deposition has been shown to produce single phase $HfCo_7$ and Zr_2Co_{11} nanoparticles that are smaller than 10 nm, without the requirement of a high-temperature annealing.[25, 26] For example, the TEM micrograph (figure 6(a)) and the corresponding particle size histogram of $Co_{89}Hf_{11}$ nanoparticles (top inset of figure 6(a)) show a narrow size distribution with an average particle size of about 7.7 nm and a standard deviation $\sigma/d \approx 0.17$. In addition, a high-resolution TEM image of a single nanoparticle reveals a high degree of crystalline ordering by showing the lattice fringes (bottom inset). In the case of the cluster deposition method, the growth of nanoparticles occurs via a nonequilibrium gas-aggregation process in a dc plasma-discharge region, where the sputtered atoms gain sufficient energy via collisions with ions to form ordered nanoparticles with high-anisotropy structures.[25, 26, 31, 38] XRD measurements were used to investigate the composition-dependent phase changes in $Co_{100-x}Hf_x$ nanoparticles.

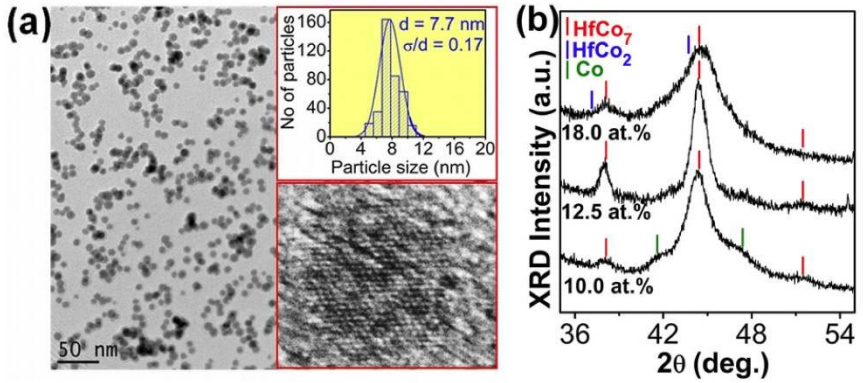

Figure 6. Structural properties of $Co_{100-x}Hf_x$ nanoparticles. (a) TEM image for $Co_{89}Hf_{11}$ nanoparticles. The corresponding particle size histogram (top) and a high-resolution image of a single nanoparticle (bottom) are given as insets. (b) XRD patterns. The standard XRD peak positions for orthorhombic $HfCo_7$, cubic HfCo2, and hcp-Co are given as red, blue, and green vertical lines, respectively.[24, 33, 34, 39]

Figure 6(b) shows the XRD patterns for $Co_{100-x}Hf_x$ nanoparticle films having different compositions. The standard XRD data for orthorhombic $HfCo_7$, cubic HfCo2 and hcp-Co are given as red, blue, and green vertical lines, respectively, in figure 6(b).[24, 33, 34, 39] For x = 10, the XRD patterns show a mixture of Co and $HfCo_7$. The $Co_{100-x}Hf_x$ nanoparticles are predominantly orthorhombic $HfCo_7$ for $11.0 \leq x \leq 14.1$ as shown in the case of the XRD pattern of $Co_{87.5}Hf_{12.5}$ nanoparticles. For high values of x (15.6 and 18), an additional weak and broad hump appears at around $2\theta \approx 43.5°$ as shown in the case of $Co_{82}Hf_{18}$ nanoparticles, which is close to the standard position of the most intense diffraction peak of the cubic Co_2Hf.

Generally the easy axes of nanoparticles are aligned using a magnetic field during the crystallization/deposition process to improve M_r.[25, 26, 30, 40–43] In the present study, the stabilization of high-anisotropy crystal structures was directly achieved in the cluster-deposited nanoparticles without a subsequent high-temperature annealing, and this is an important processing step to align the easy axes prior to deposition. For magnetic characterization, as schematically shown in figure 7(a), $Co_{100-x}Hf_x$ nanoparticles are aligned with a magnetic field of about 5 kOe prior to deposition on Si(001) substrate as described elsewhere.[25, 26] As compared to the melt-spun $Co_{100-x}Hf_x$ ribbons, the aligned nanoparticle films show high H_c values at 300 K (figure 7(b)) and also exhibit a high $M_r/M_s \approx 0.85$ (not shown in figure 7(b)) along the easy axis. We also estimated the easy-axis distribution in the aligned nanoparticles from $M_r/M_s \approx 0.85$ by following standard methods.[25, 44–46] The aligned $HfCo_7$ nanoparticles show a narrow normalized easy-axis probability distribution $p(\theta)$ with a half width at half maximum of about 26° (figure 7(c)), where θ is the angle between the easy axis and the direction of the applied field during the measurement (or the direction of the alignment field in figure 7(a)). In addition, this analysis also shows that about 70% of nanoparticles are within the alignment angles smaller than 30°.

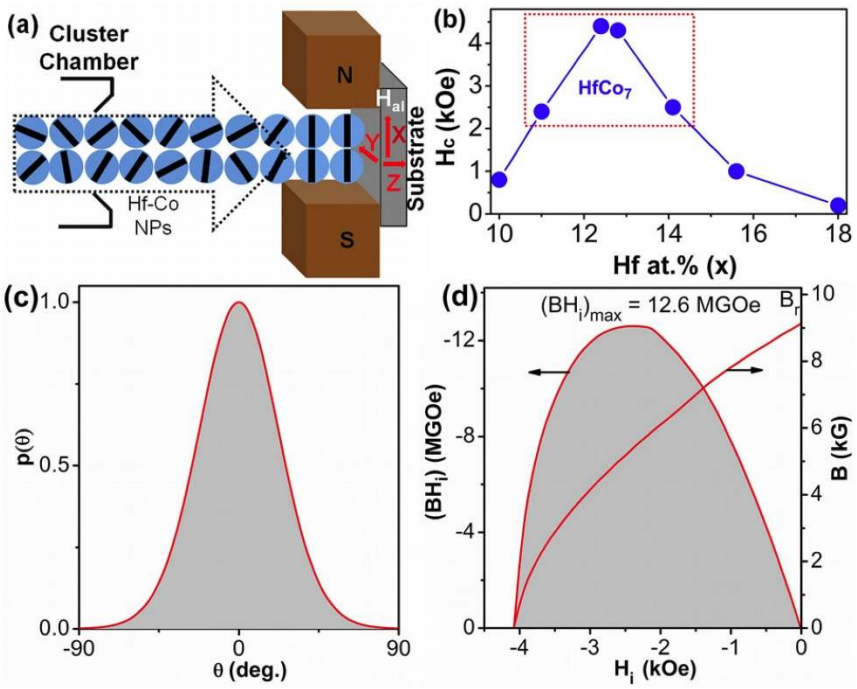

Figure 7. Easy-axis alignment of $Co_{100-x}Hf_x$ nanoparticles: (a) experimental setup showing the schematic of the alignment.[25, 26] (b) Room temperature coercivities H_c measured along the easy axis. (c) The normalized easy-axis distribution function $p(\theta)$ for $HfCo_7$ nanoparticle films, where θ is the angle between the easy axis and applied field during the measurement (direction of the alignment field H_{al}). (d) The room-temperature B and BH_i curves as a function of H_i for $HfCo_7$.

The easy-axis alignment of $HfCo_7$ nanoparticles leads to a high remanent magnetic field induction $B_r = 9.1$ kG and a high $(BH_i)_{max} = 12.6$ MGOe as shown in figure 7(d). $N = 0.15$ was used to obtain H_i for $HfCo_7$ nanoparticle films and this is estimated by comparing the slopes (micromagnetic susceptibilities) of in-plane and out-of-plane $M(H)$ curves of isotropic $HfCo_7$ thin-film samples.[5, 6, 47] Note that the packing fraction of nanoparticles is generally below full compaction in the films,[17, 25] and thus $(BH_i)_{max}$ obtained for the $HfCo_7$ nanoparticle film from figure 7(d) is a nominal value. However, the volume fraction of magnetic materials in the cluster-deposited films have been shown to be improved via forming exchange-coupled nanocomposites by code-positing high-anisotropy nanoparticles and a soft magnetic phase.[25] Besides achieving a packing fraction close to a full compaction, the energy products also improved due to the exchange coupling between the hard and soft phases.[25]

Although the cluster-deposited $HfCo_7$ nanoparticles exhibit a higher energy product of about 12.6 MGOe than that of the best alnico magnet, this value is less than the maximum achievable energy product of about 34.8 MGOe in $HfCo_7$. The Stoner-Wohlfarth model predicts a maximum possible $H_c \approx 2K_1/M_s$ for easy-axis aligned noninteracting single-

domain particles.[5, 6, 48] Thus, for $HfCo_7$ nanoparticles having $K_1 \approx 19.4$ Mergs cm^{-3}; H_c should be far higher than the observed maximum value of 4.4 kOe. The aligned $HfCo_7$ nanoparticles are, however, dense-packed in the cluster-deposited films, and this leads to the interparticle interactions, which subsequently decreases H_c. Thus the present results show that it is essential to minimize the interparticle interactions in nanoparticles to increase the energy products approaching theoretical maximum. One of the possible ways to achieve this goal is to fabricate idealized nanostructures in which the easy-axis aligned nanoparticles are isolated by a nonmagnetic layer, which can maintain a high H_c by pinning the domain-wall motion.[9, 11, 49, 50] Since the energy product also directly depends on the packing fraction of magnetic phases, it is also important to maintain the thickness of the nonmagnet layer to be as small as possible (typically a monolayer). This study shows that $(BH)_{max}$ value close to the theoretical maximum can be achieved only by obtaining nearly perfect crystallographic alignment of the easy magnetization axes, controlling the exchange interactions between the magnetic grains, and substantially reducing the nonmagnetic phases or achieving a complete packing of magnetic phases.[8–11]

4. Conclusions

Nanostructured $Co_{100-x}TM_x$ alloys (TM = Hf, Zr) having $10 \le x \le 18$ were prepared using melt-spinning and cluster-deposition methods. XRD studies show that the nonequilibrium growth conditions facilitate the stability of the intermetallic $HfCo_7$ and Zr_2Co_{11} phases for extended composition ranges. The results provide further insights to understand the formation of the metastable phases and tailor their permanent-magnet properties. Nanostructured rare-earth-free Co-rich alloys exhibit high Curie temperatures of above 750 K and also show a maximum energy product of about 12.6 MGOe in the case of the cluster-deposited $HfCo_7$ nanoparticle film, which is high for permanent-magnet alloys not containing critical rare-earth elements and expensive Pt. The nanostructured alloys can be exploited in applications that require magnets with energy products in the intermediate range between alnico and RE-containing materials.

Acknowledgments – This work is supported by the US Department of Energy DOE/BES (Grant No. DEFG0204ER46152). Thanks are due to V R Shah and X Z Li for helpful discussions.

References

[1] Jacoby, M. 2013. *Chem. Eng. News* 91, 23.

[2] Kramer, M. J., McCallum, R. W., Anderson, I. A., and Constantinides, S. 2012. *JOM* 64, 752.

[3] Jones, N. 2011. *Nature* 472, 22.

[4] Kramer, D. 2010. *Phys. Today* 63, 22.

[5] Skomski, R. 2008. *Simple Models of Magnetism* (Oxford: Oxford University Press).

[6] Coey, J. M. D. 2009. *Magnetism and Magnetic Materials* (Cambridge: Cambridge University Press).

[7] Kneller, E. 1962. *Ferromagnetism* (Berlin: Springer).

[8] Sellmyer, D. J. 2002. *Nature* 420, 374.

[9] Balamurugan, B., Sellmyer, D. J., Hadjipanayis, G. C., and Skomski, R. 2012. *Scr. Mater*. 67, 542. Sellmyer, D. J., and Balamurugan, B. 2012. *Magnetics Technology International* (Derking: UKIP Media & Events, Ltd.), pp. 40–44.

[10] Poudyal, N., and Liu, J. P. 2013. *J. Phys. D: Appl. Phys.* 46, 043001.

[11] Liu, Y., George, T. A., Skomski, R., and Sellmyer, D. J. 2011. *Appl. Phys. Lett.* 99, 172504.

[12] Coey, J. M. D. 2012. *Scr. Mater.* 67, 524.

[13] Balke, B., Fecher, G. H., Winterlik, J., and Felser, C. 2007. *Appl.Phys. Lett.* 90, 152504.

[14] Park, J. H., Hong, Y. K., Bae, S., Lee, J. J., Jalli, J., Abo, G. S., Neveu N., Kim, S. G., Choi, C. J., and Lee, J. G. 2010. *J. Appl. Phys.* 107, 09A731.

[15] Yang, J. B., Kamaraju, K., Yelon, W. B., James, W. J., Cai, Q., and Bollero, A. 2001. *Appl. Phys. Lett.* 79, 1846.

[16] Rao, N. V. R., Gabay, A. M., and Hadjipanayis, G. C. 2013. *J. Phys. D: Appl. Phys.* 46, 062001.

[17] Cui, W., Takahashi, T., and Hono, K. 2012. *Adv. Mater.* 48, 6530.

[18] Zeng, H., Li, J., Liu, J. P., Wang, Z. L., and Sun, S. 2002. *Nature* 420, 395. Takahashi, Y. K., Seki, T. O., Hono, K., Shima, T., and Takanashi, K. 2004. *J. Appl. Phys.* 96, 475. Jeong, S., McHenry, M. E., and Laughlin, D. E. 2001. *IEEE Trans. Magn.* 37, 1309.

[19] Zhang, W. Y., Li, X. Z., Valloppilly, S. R., Skomski, R., Shield, J. E., and Sellmyer, D. J. 2013. *J. Phys. D: Appl. Phys.* 46, 135004.

[20] Burzo, E., Grossinger, R., Hundergger, P., Kirchmayr, H. R., Krewenka, R., Mayerhofer, O., and Lemarie, R. 1991. *J. Appl. Phys.* 70, 6550. Ivanova, G. V., Shchegoleva, N. N., and Gabay, A. M. 2007. *J. Alloys Compounds* 432, 135. Hou, Z., Xu S., Zhang, J., Wu, C., Liu, D., Su, F., and Wang, W. 2013. *J. Alloys Compounds* 555, 28. Saito, T., and Itakura, M. 2013. *J. Alloys Compounds* 572, 124. Hou, Z., Wang, W., Xu, S., Zhang, J., Wu, C., and Su, F. 2012. *Physica B* 407, 1047.

[21] Gabay, A. M., Zhang, Y., and Hadjipanayis, G. C. 2001. *J. Magn. Magn. Mater.* 236, 41.

[22] Ishikawa, T., and Ohmori, K. 1990. *IEEE Trans. Magn.* 26, 1370.

[23] Saito, T. 2003. *Appl. Phys. Lett.* 82, 2305.

[24] Das, B., Balamurugan, B., Kumar, P., Skomski, R., Shah, V. R., Shield, J. E., Kashyap, A., and Sellmyer, D. J. 2013. *IEEE Trans. Magn.* 49, 3215.

[25] Balamurugan, B., Das, B., Skomski, R., Zhang, W. Y., and Sellmyer, D. J. 2013. *Adv. Mater.* doi:10.1002/adma201302704

[26] Balamurugan, B., Das, B., Shah, V. R., Skomski, R., Li, X. Z., and Sellmyer, D. J. 2012. *Appl. Phys. Lett.* 101, 122407.

[27] McGuire, M. A., Rios, O., Ghimire, N. J., and Koehler, M. 2012. *Appl. Phys. Lett.* 101, 202401.

[28] Okamoto, H. 2000. *Phase Diagram of Binary Alloys* (Materials Park, OH: ASM), p. 248.

[29] Okamoto, H. 2000. *Phase Diagram of Binary Alloys* (Materials Park, OH: ASM), p. 263.

[30] Qiu, J. M., and Wang, J. P. 2006 *Appl. Phys. Lett.* 89, 222506. Wang, J. P., Qiu, J. M., Taton, T. A., and Kim, B. 2006. *IEEE Trans. Magn.* 42, 3042.

[31] Balasubramanian, B., Skomski, R., Li, X. Z., Valloppilly, S. R., Shield, J. E., Hadjipanayis, G. C., and Sellmyer, D. J. 2011. *Nano Lett.* 11, 1747.

[32] Hadjipanayis, G. C., Sellmyer, D. J., and Brandt, B. 1981. *Phys. Rev. B* 23, 3349.

[33] 2011 *ICDD-International Center for Diffraction Data* Card No. 000150098.

[34] 2013 *ICDD-International Center for Diffraction Data* Card No. 040033881.

[35] Skomski, R. 2003. *J. Phys.: Condens. Matter* 15, R841.

[36] Ashcroft, N. W., and Mermin, N. D. 1976. *Solid State Physics* (New York: Holt, Rinehart, and Winston).

[37] Bloch, F. 1930 *Z. Phys.* 61, 206.

[38] Patterson, M. M., Cochran, A., Ferina, J., Rui, X., Zimmerman, T. A., Sun, Z., Kramer, M. J., Sellmyer, D. J., and Shield, J. E. 2010. *J. Vac. Sci. Technol. B* 28, 273.

[39] 2011 *ICDD-International Center for Diffraction Data* Card No. 010894308.

[40] Yu, Y., Mendoza-Gracia, A., Ning, B., and Sun, S. 2013. *Adv. Mater.* 25, 3090.

[41] Kang, S., Shi, S., Jia, Z., Thompson, G. B., Nikles, D. E., Harrell, J. W., Li, D., Poudyal, N., Nandwana, V., and Liu, J. P. 2007. *J. Appl. Phys.* 101, 09J113.

[42] Kang, S., Jia, Z., Shi, S., Nikles, D. E., and Harrell, J. W. 2005. *Appl. Phys. Lett.* 86, 062503.

[43] Harrel, J. W., Kang, S., Jia, Z., Nikles, D. E., Chantrell, R., and Satoh, A. 2005. *Appl. Phys. Lett.* 87, 202508.

[44] Le Roy, D., Morel, R., Brenac, A., and Notin, L. 2011. *J. Magn. Magn. Mater.* 323, 127.

[45] Néel, L., Pauthenet, R., Rimet, G., and Giron, V. S. 1960. *J. Appl. Phys.* 31, 27S.

[46] Givord, D., Lignard, A., Perrier de la Bathie, R., Tenaud, P., and Viadieu, T. 1985. *J. Physique Colloq.* 6, 313.

[47] Zheng, G., Pardavi-Horvath, M., Huang, X., Keszei, B., and Vandlik, J. 1996. *J. Appl. Phys.* 79, 5742.

[48] Wohlfarth, E. P. 1958. *J. Appl. Phys.* 29, 595.

[49] Xu, Y., Yan, M. L., Zhou, J., and Sellmyer, D. J. 2005. *J. Appl. Phys.* 97, 10J320.

[50] Rui, X., Shield, J. E., Sun, Z., Yue, L., Xu, Y., Sellmyer, D. J., Liu, Z., and Miller, D. J. 2006. *J. Magn. Magn. Mater.* 305, 76. Rui, X., Shield, J. E., Sun, Z., Xu, Y., and Sellmyer, D. J. 2006. *Appl. Phys. Lett.* 89, 122509.